

Improved limits on solar axions and bosonic dark matter from the CDEX-1B experiment using the profile likelihood ratio method

Y. Wang,^{1,2} Q. Yue,^{1,*} S.K. Liu,^{3,†} K.J. Kang,¹ Y.J. Li,¹ H.P. An,^{1,2} J.P. Chang,⁴ J.H. Chen,⁵ Y.H. Chen,⁶ J.P. Cheng,¹ W.H. Dai,¹ Z. Deng,¹ X.P. Geng,¹ H. Gong,¹ P. Gu,³ X.Y. Guo,⁶ H.T. He,³ L. He,⁴ S.M. He,⁶ J.W. Hu,¹ H.X. Huang,⁷ T.C. Huang,⁸ L.P. Jia,¹ H.B. Li,⁵ H. Li,⁴ M.X. Li,³ J.M. Li,¹ J. Li,¹ X. Li,⁷ X.Q. Li,⁹ Y.L. Li,¹ B. Liao,¹⁰ F.K. Lin,⁵ S.T. Lin,³ Y.D. Liu,¹⁰ Y.Y. Liu,¹⁰ Z.Z. Liu,¹ H. Ma,¹ Q.Y. Nie,¹ J.H. Ning,⁶ H. Pan,⁴ N.C. Qi,⁶ C.K. Qiao,³ J. Ren,⁷ X.C. Ruan,⁷ V. Sharma,^{5,11} Z. She,¹ L. Singh,^{5,11} M.K. Singh,^{5,11} T.X. Sun,¹⁰ C.J. Tang,³ W.Y. Tang,¹ Y. Tian,¹ G.F. Wang,¹⁰ L. Wang,¹² Q. Wang,¹ Z. Wang,³ H.T. Wong,⁵ S.Y. Wu,⁶ Y.C. Wu,¹ H.Y. Xing,³ Y. Xu,⁹ T. Xue,¹ Y.L. Yan,³ L.T. Yang,¹ N. Yi,¹ C.X. Yu,⁹ H.J. Yu,⁴ J.F. Yue,⁶ X.H. Zeng,⁶ M. Zeng,¹ Z. Zeng,¹ B.T. Zhang,¹ F.S. Zhang,¹⁰ L. Zhang,³ Z.Y. Zhang,¹ M.G. Zhao,⁹ J.F. Zhou,⁶ Z.Y. Zhou,⁷ and J.J. Zhu³

(CDEX Collaboration)

¹Key Laboratory of Particle and Radiation Imaging (Ministry of Education) and Department of Engineering Physics, Tsinghua University, Beijing 100084

²Department of Physics, Tsinghua University, Beijing 100084

³College of Physics, Sichuan University, Chengdu 610064

⁴NUCTECH Company, Beijing 100084

⁵Institute of Physics, Academia Sinica, Taipei 11529

⁶YaLong River Hydropower Development Company, Chengdu 610051

⁷Department of Nuclear Physics, China Institute of Atomic Energy, Beijing 102413

⁸Sino-French Institute of Nuclear and Technology, Sun Yat-sen University, Zhuhai, 519082

⁹School of Physics, Nankai University, Tianjin 300071

¹⁰College of Nuclear Science and Technology, Beijing Normal University, Beijing 100875

¹¹Department of Physics, Banaras Hindu University, Varanasi 221005

¹²Department of Physics, Beijing Normal University, Beijing 100875

(Dated: April 27, 2021)

We present the improved constraints on couplings of solar axions and more generic bosonic dark matter particles using 737.1 kg-days of data from the CDEX-1B experiment. The CDEX-1B experiment, located at the China Jinping Underground Laboratory, primarily aims at the direct detection of weakly interacting massive particles using a p-type point-contact germanium detector. We adopt the profile likelihood ratio method for analysis of data in the presence of backgrounds. An energy threshold of 160 eV was achieved, much better than the 475 eV of CDEX-1A with an exposure of 335.6 kg-days. This significantly improves the sensitivity for the bosonic dark matter below 0.8 keV among germanium detectors. Limits are also placed on the coupling $g_{Ae} < 2.48 \times 10^{-11}$ from Compton, bremsstrahlung, atomic-recombination and de-excitation channels and $g_{AN}^{eff} \times g_{Ae} < 4.14 \times 10^{-17}$ from a ⁵⁷Fe M1 transition at 90% confidence level.

I. INTRODUCTION

For the charge-parity (CP) problem of strong interactions, the Peccei-Quinn (PQ) mechanism [1] is still the most compelling solution in which a new kind of U(1) symmetry would be spontaneously broken at large energy scale f_A . After this original solution to the CP conservation in QCD, a new Nambu-Goldstone boson called axion is proposed later by Weinberg [2] and Wilczek [3] through the PQ symmetry. Axions are pseudoscalar particles with properties closely related to those of neutral pions and their mass m_A is fixed by the scale f_A of the PQ symmetry breaking, $m_A \approx 6 \text{ eV} (10^6 \text{ GeV}/f_A)$. The range of scale f_A can not be restricted by theory but the order of the electroweak scale has been excluded by experiments. At a higher symmetry-breaking

energy scale, ‘invisible’ axion models such as hadronic model KSVZ (Kim-Shifman-Vainstein-Zakharov) [4, 5] and non-hadronic model DFSZ (Dine-Fischler-Srednicki-Zhitnitskii) [6, 7] are still allowed. Another interest in this paper is more general bosonic dark matter (DM) like axion-like particles (ALPs) and vector bosonic DM, which also have couplings to electrons.

Several experiments have reported the corresponding results [8–23] using the mechanism arising from the couplings to electrons:

$$A(B) + e + Z \rightarrow e + Z, \quad (1)$$

where A and B represent axion and bosonic DM respectively. This effect is similar to photoelectric effect just replacing photon with axion or bosonic DM.

The China Dark Matter Experiment (CDEX) is primarily designed to carry out direct detection of low mass weakly interacting massive particles (WIMPs) with p-type point contact germanium detectors (PPCGe) at China Jinping Underground Laboratory (CJPL) [24–30]. With a vertical rock overburden of 2.4 km, CJPL

* Corresponding author: yueq@mail.tsinghua.edu.cn

† Corresponding author: liusk@scu.edu.cn

provides a measured muon flux of $61.7 \pm 11.7 \text{ y}^{-1} \text{ m}^{-2}$ [31]. Besides the WIMPs constraints [32, 33], the axion searches results from the CDEX-1A experiment based on the 335.6 kg-days of data has been reported before [18]. Using a PPCGe with fiducial mass of 915 g, a physics threshold of 475 eV [33] was achieved for CDEX-1A. Focused on the lower energy threshold, a new 1 kg-scale PPCGe detector has been designed and named ‘CDEX-1B’ based on the experience from our previous prototype detector used in CDEX-1A.

In this paper, We report the solar axion, ALPs and vector bosonic DM searches results from the CDEX-1B experiment based on the 737.1 kg-days of data, which is the same data set in the analysis of WIMP search [34], annual modulation [30] and Migdal effects [29]. Also we describe the statistical model with profile likelihood ratio method applied to this data.

II. AXION SEARCHES WITH CDEX-1B

A. CDEX-1B setup and overview

The CDEX-1B experiment adopts one 939 g single-element PPCGe crystal with dead layer of 0.88 ± 0.12 mm [35]. Outside of the PPCGe detector is the passive shielding system and the detailed information is described in Ref. [34]. A well-shaped cylindrical NaI(Tl) crystal surrounding the PPCGe detector is used as the anti-Compton detector. The coincidence events both in germanium and NaI(Tl) crystals denoted as AC⁺ are discarded to depress the γ background.

The schematic diagram of electronics and data acquisition (DAQ) system is shown in Ref. [34]. Four identical energy-related signals were out of the p⁺ point-contact electrode after a pulsed-reset feedback preamplifier. Two of them were distributed into the shaping amplifiers at 6 μs (SA_{6 μs}) and 12 μs (SA_{12 μs}) shaping time for low energy region (0-12 keV). The output of SA_{6 μs} provided the system trigger of the DAQ. The other two outputs were fed into timing amplifiers (TA) which provide the accurate time information. One with high gain (TA₁) is limited to medium energy region (0-20 keV), and the other one with low gain (TA₂) for high energy can reach 1.3 MeV. The energy resolution of TA₁ output is similar to the SA_{6 μs , 12 μs} . As a result, the spectrum below 12 keV is from SA_{6 μs} and above 12 keV is from TA₁ in our analysis. The energy resolution (σ) from SA_{6 μs} at 1.3 keV is about 44 eV.

B. Particle sources

1. Solar Axions

The sun is a potential source of axions and in this article we concentrate on two different mechanisms.

The first important source is the 14.4 keV monochromatic axions from the M1 transition of the ⁵⁷Fe in the sun, i.e. ⁵⁷Fe* \rightarrow ⁵⁷Fe + A, due to the stability and the large abundance of ⁵⁷Fe in the sun.

The Lagrangian coupling axions to nucleons is [12]:

$$\mathcal{L} = i\bar{\psi}_N \gamma_5 (g_{AN}^0 + g_{AN}^3 \tau_3) \psi_N \phi_A, \quad (2)$$

where ψ_N is the nucleon isospin doublet, ϕ_A is the axion field, and τ_3 is Pauli matrix. g_{AN}^0 and g_{AN}^3 are the model-dependent isoscalar and isovector axion-nucleon coupling constants [36, 37]. Introducing $g_{AN}^{\text{eff}} \equiv (-1.19g_{AN}^0 + g_{AN}^3)$ as the effective nuclear coupling adapted to the case of ⁵⁷Fe, the corresponding axion flux is given by [12, 38]:

$$\Phi_{14.4} = \left(\frac{\kappa_A}{\kappa_\gamma} \right)^3 \times 4.56 \times 10^{23} (g_{AN}^{\text{eff}})^2 \text{ cm}^{-2} \text{ s}^{-1}, \quad (3)$$

where κ_A and κ_γ are the momenta of the outgoing axion and photon respectively. Given the axion-nucleon couplings g_{AN}^0 and g_{AN}^3 for specific models such as DFSZ and KSVZ, the axion flux can be evaluated.

Another important sources are from the Compton-like scattering (C), axion-bremsstrahlung (B), atomic-recombination (R) and atomic-deexcitation (D) processes. Their corresponding effective Lagrangian is given by [12]:

$$\mathcal{L} = ig_{Ae} \bar{\psi}_e \gamma_5 \psi_e \phi_A, \quad (4)$$

where g_{Ae} is the dimensionless axion-electron coupling constant. Its flux depends on the g_{Ae}^2 :

$$\begin{aligned} \frac{d\Phi_{CB}}{dE_A} &= \frac{d\Phi_C}{dE_A} + \frac{d\Phi_B}{dE_A} \\ &= g_{Ae}^2 \times 1.33 \times 10^{33} E_A^{2.987} e^{-0.776E_A} \\ &\quad + g_{Ae}^2 \times 2.63 \times 10^{35} E_A e^{-0.77E_A} \frac{1}{1 + 0.667E_A^{1.278}}, \end{aligned} \quad (5)$$

where the units of fluxes are $\text{cm}^{-2} \text{ s}^{-1} \text{ keV}^{-1}$ and axion energy E_A is in unit of keV. For the atomic-recombination and atomic-deexcitation process, the tabulated spectrum in Ref. [39] is used. As discussed in Ref. [39], the flux is valid for relativistic axion; hence, we consider only the axion mass below 1 keV.

The axion-electron coupling is depended on models. In the DFSZ model, the coupling is proportional to $\cos^2 \beta$, where $\tan \beta$ is the ratio of the two Higgs vacuum expectation values. In the KSVZ model, it depends on E/N , the ratio of electromagnetic to color anomalies. $E/N = 0$ and $\cos^2 \beta = 1$ are used in this analysis [12].

2. Bosonic Dark Matter

The main cosmological interest in bosonic particles such as ALPs and vector bosonic DM arises from their possible role as the dominant component of dark matter, the nature of which is still unknown. The absorption via ionization or excitation of an electron in target

atom makes bosonic DM experimentally interesting and PPCGe detectors have advantages to study bosonic DM due to their excellent energy resolution, sub-keV threshold and low radioactivity background.

Assuming that these bosonic particles constitute all of the galactic dark matter, we get the total average flux of dark matter axions on Earth:

$$\begin{aligned}\Phi_{\text{DM}} &= \rho_{\text{DM}} \cdot v_A / m_A \\ &= 9.0 \times 10^{15} \times \beta \cdot \left(\frac{\text{keV}}{m_A} \right) \text{cm}^{-2} \text{s}^{-1},\end{aligned}\quad (6)$$

where $\rho_{\text{DM}} \sim 0.3 \text{ GeV}/\text{cm}^3$ is the dark matter halo density [40], m_A is the axion mass, v_A is the mean axion velocity distribution with respect to the Earth and β is the ratio of the axion velocity to the speed of light for cold dark matter. This flux is independent of any axion coupling.

C. Particle interactions in CDEX-1B

The axion detection channel studied in this paper is the axio-electric effect illustrated in Eq. (1). The axio-electric cross-section as described in Ref. [41–43] is given by:

$$\sigma_{Ae}(m_A) = \sigma_{pe}(m_A) \frac{g_{Ae}^2}{\beta} \frac{3m_A^2}{16\pi\alpha m_e^2} \left(1 - \frac{\beta^2}{3} \right), \quad (7)$$

where $\sigma_{pe}(m_A)$ is the photo-electric cross-section for germanium in the unit of barns/atom, m_A is the mass of axion, α is the fine structure constant, m_e is the electron mass and β is the ratio of the axion velocity to the speed of light. The expected axion event rates of CBRD process and ^{57}Fe under the consideration of energy resolution are displayed in the Fig. 1.

In the situation of ALPs in cold dark matter model ($\beta \approx 10^{-3}$), the coupling to electrons is the same as in the case of solar axions. For the vector bosonic DM, the absorption cross section σ_{abs} can be written as:

$$\sigma_{\text{abs}}(m_v) = \sigma_{pe}(m_v) \frac{\alpha'}{\alpha}, \quad (8)$$

where m_v is the mass of the vector bosonic DM, α and α' are the fine structure constant and its vector boson equivalent, respectively.

Using the parameter mentioned above, the interaction rate in the direct detection experiment can be written as:

$$R = 1.2 \times 10^{43} A^{-1} g_{Ae}^2 m_A \sigma_{pe}(m_A) \quad (9)$$

for ALPs and

$$R = 4 \times 10^{47} A^{-1} \frac{\alpha'}{\alpha} m_v^{-1} \sigma_{pe}(m_v) \quad (10)$$

for vector bosonic DM, where A is mass number of germanium. The expected rates of these two kinds of particles are shown in Fig. 2.

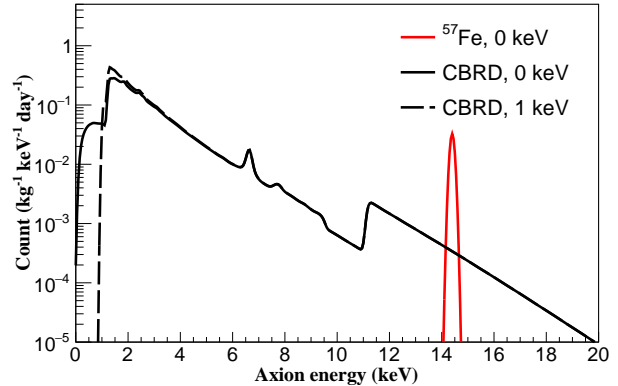


FIG. 1. The expected axion event rates of CBRD process at the mass of 0 keV and 1 keV, and ^{57}Fe 14.4 keV axion at the mass of 0 keV. Here the axion couplings are $g_{Ae} = 2 \times 10^{-11}$ and $g_{AN}^{eff} \times g_{Ae} = 2 \times 10^{-17}$.

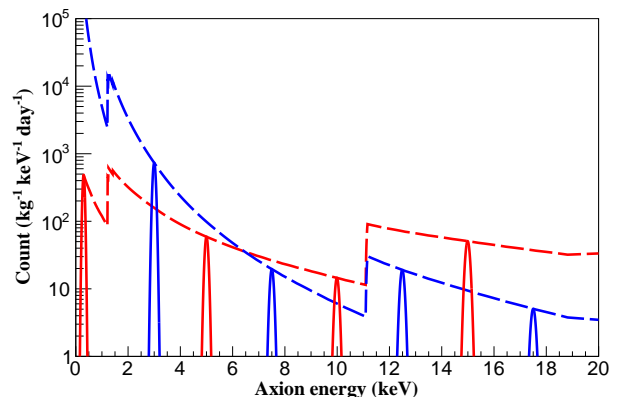


FIG. 2. The expected event rate of ALPs (red solid line) and vector bosonic DM (blue solid line) at different masses. The red dashed line is the maximum event rate of ALPs Gaussian distributions versus their masses, while the blue dashed line is corresponding to vector bosonic DM. The couplings used here are $g_{Ae} = 2 \times 10^{-11}$ and $\alpha'/\alpha = 5 \times 10^{-25}$. The widths of these peaks are determined by the energy resolution.

III. DATA ANALYSIS

A. Data Selection

As discussed in earlier analysis [34], the background spectrum is derived by the following steps:

1. Stability check, removing the time periods of calibration or other testing experiments.
2. Anti-Compton (AC) veto, discarding the events in coincidence with the AC detector and retaining the anti-coincidence events.
3. Basic cuts, removing the electronic noise through getting rid of the abnormal pulses and spurious signals.

4. Bulk and surface event selection, rejecting the surface events by pulse shape analysis using their characteristic slower rise time.

Depicted in Fig. 3 are the trigger efficiency as well as the selection efficiency with energy including those from the selection of physics vs electronic noise events, AC vetos and DAQ dead time. The trigger efficiency is derived from the calibration sources in coincidence with AC detector [34]. The selection efficiencies are derived by events due to random triggers, the AC tagged events from calibration sources and in situ background. An improved Ratio Method, which is based on the bulk/surface rise time distribution probability density functions (PDFs), is developed to reject the surface events [44]. This method has been proved correctly above 160 eV. So in this analysis, 160 eV is selected as the physics analysis threshold, at which the combined efficiencies (ϵ_{eff}) including trigger and selection is 17%.

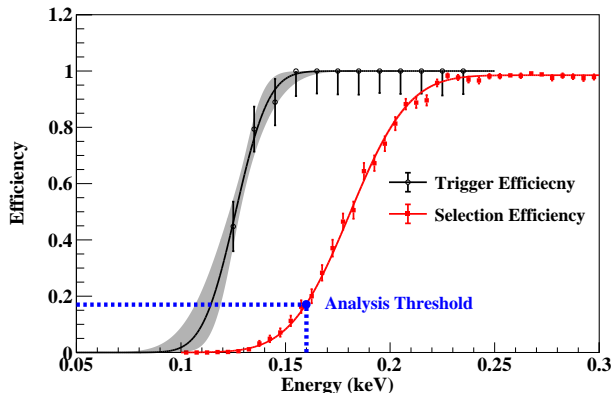


FIG. 3. The trigger efficiency and selection efficiency derived from source events are depicted respectively and fitted with error functions. The shadow parts represent the 1σ error bands.

B. Background and Understanding

With an exposure of 737.1 kg-days, the bulk spectrum from 160 eV up to 20 keV after data selection and efficiency correction is displayed in Fig. 4(a). The background consists of several K-shell X-rays and their corresponding L-shell X-rays from the cosmogenic isotopes and a continuous background with a smooth, slightly increasing profile as the energy decreases [34]. Considering the low muon flux mentioned above, the contribution from muons can be neglected. The continuous background below 20 keV is expected to probably originate from the ^{238}U , ^{232}Th and ^{40}K in the materials in the vicinity of the PPCGe detector, radon gas penetrating through shielding and cosmogenic ^3H in the crystal. A detailed modeling of the continuous background is beyond this work and will be studied in our future work.

However, axion analysis is not sensitive to the accurate background assumption because the signatures of axion are significantly different from the continuous background. As can be seen from Fig. 2, the signal signatures of ^{57}Fe and bosonic DM are monochromatic and of Gaussian distribution with widths determined by the energy resolution. As to the continuous CBRD solar axion, a saw-tooth-like profile arises between 0.9 keV and 1.6 keV considering the axion mass below 1 keV. So in the following fitting procedure, the background model can be described by a continuous background plus the peaks from K/L-shell X-rays. Benefiting from the low threshold and excellent energy resolution of CDEX-1B, the L-shell X-ray peaks at low energy region can be clearly distinguished. Therefore, in the background model, the amplitude of the K-shell X-ray peaks and the corresponding L-shell X-ray peaks are limited by each other using the K/L-shell X-ray ratios mentioned in Ref. [45, 46]. In the ultra low energy region around the threshold, M-shell X-rays are also taken into consideration in the background model.

The corrected surface spectrum derived from Ratio Method is depicted in Fig. 4(b). Note that, as will be clear in next section, the likelihood analysis makes use of both the bulk and surface data.

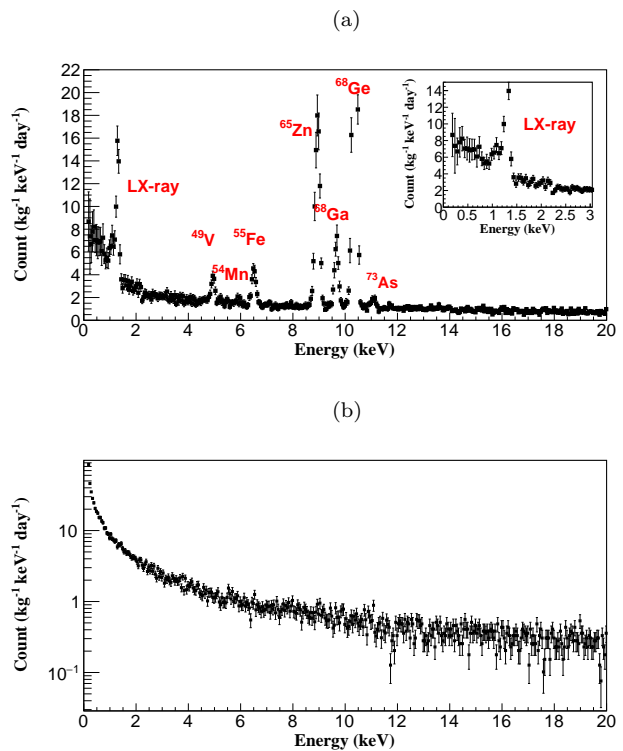


FIG. 4. (a) The corrected bulk spectrum from 160 eV to 20 keV. (b) The corrected surface spectrum from 160 eV up to 20 keV.

C. Profile likelihood Analysis

A profile likelihood analysis, as described in Ref. [47], is adopted to derive the constraints and the test statistics is:

$$q_\mu = \begin{cases} -2\ln \left(\frac{L(\mu, \hat{\theta})}{L(\hat{\mu}, \hat{\theta})} \right) & \mu \geq \hat{\mu} \\ 0 & \mu < \hat{\mu}, \end{cases} \quad (11)$$

where L is the likelihood function. Quantity μ is a parameter corresponding to the strength of signals and θ denotes all of the nuisance parameters. The quantity $\hat{\theta}$ denotes the value of θ that maximizes L for the specified μ , while the denominator is the maximized likelihood function, i.e. μ and θ are their maximum-likelihood estimators. To obtain the 90% C.L. bounds on the signal strengths μ , the asymptotic formulas are used to calculate the probability distribution functions (PDFs), i.e.,

$$f(q_\mu|\mu') = \Phi\left(\frac{\mu' - \mu}{\sigma}\right)\delta(q_\mu) + \frac{1}{2} \frac{1}{\sqrt{2\pi}} \frac{1}{\sqrt{q_\mu}} \exp\left[-\frac{1}{2}\left(\sqrt{q_\mu} - \frac{\mu - \mu'}{\sigma}\right)^2\right], \quad (12)$$

where $f(q_\mu|\mu')$ is the PDF of the test statistic q_μ under the signal strength hypothesis μ' , while σ is the corresponding standard deviation [47]. Since downward fluctuations of background might lead to much stringent exclusion results, we used the CL_s method [48] to get rid of this effect. The 90% up limits μ_{up} are defined as:

$$\frac{1 - F(q_\mu|\mu)_{\text{up}}}{1 - F(q_\mu|0)_{\text{up}}} = 10\%, \quad (13)$$

where F is the cumulative distribution function of the test statistic.

1. Likelihood Function

The specific full likelihood function \mathcal{L} we used in this analysis is written as a product of three terms:

$$\mathcal{L} = \mathcal{L}_1(\nu_A, \nu_b, \nu_s, g_b, g_s, \varepsilon_{\text{eff}}; m_A) \times \mathcal{L}_2(\varepsilon_{\text{eff}}(E)) \times \mathcal{L}_3(t_b, t_s), \quad (14)$$

the parameter of interest becomes the number of fitted axion event number denoted ν_A which is related to the axion-electron coupling strength g_{Ae} , whereas $\nu_b, \nu_s, g_b, g_s, \varepsilon_{\text{eff}}$ are considered as the main nuisance parameters.

$$\mathcal{L}_1 = \prod_{j=1}^{N_\tau} \prod_{i=1}^{N_E} \text{Poisson}[n_{ij} | (g_b(\tau_j; E_i; t_b) \cdot \varepsilon_{\text{eff}}(E_i) \cdot N_{i,\text{bulk}} + g_s(\tau_j; E_i; t_s) \cdot \varepsilon_{\text{eff}}(E_i) \cdot N_{i,\text{surf}})] \quad (15)$$

describes the measurement of the detector. Here we projected all the data into the Energy versus rise-time 2-dimension grids, as depicted in Fig. 5(a). The n_{ij} is the measured event number both in the energy spectrum bin E_i and the rise time spectrum bin τ_j . $g_b(\tau; E_i; t_b)$ and $g_s(\tau; E_i; t_s)$ are the distributions of rise-time at the condition of a certain energy bin i from bulk event and surface event respectively, i.e., $g_k(\tau_j; E_i) = \mu_k(\tau_j; E_i) + t_k \cdot \sigma_{k,ij}$, $k = \text{bulk or surface}$. Normalized PDFs $\mu_k(\tau_j; E_i)$ are the best fit values derived from Ratio Method in the rise-time distribution shown in Fig. 5(b), as well as their corresponding errors $\sigma_{k,ij}$ including statistical and systematic uncertainties which have already been derived in Ref. [34, 44]. ε_{eff} described by \vec{e} refers to the combined efficiencies mentioned in the Sec. III. A:

$$\varepsilon_{\text{eff}} = \left\{ \frac{1}{2} \times [1 + \text{Erf}\left(\frac{E - e_1}{\sqrt{2}e_2}\right)] \right\}_{\text{trigger}} \times \left\{ \frac{e_3}{2} \times [1 + \text{Erf}\left(\frac{E - e_4}{\sqrt{2}e_5}\right)] \right\}_{\text{selection}} \quad (16)$$

$N_{i,\text{bulk}}$ and $N_{i,\text{surf}}$ are the expected numbers of bulk events and surface events at the certain energy bin i , respectively, which are determined by the fitting results:

$$N_{i,\text{bulk}} = \nu_b \cdot f_b(E_i) + \nu_A \cdot f_A(E_i) \\ , N_{i,\text{surf}} = \nu_s \cdot f_s(E_i). \quad (17)$$

f_b, f_A and f_s represent the PDFs of the background, the axion signal and the surface events, respectively. Each of them is normalized to unity over the energy range of the fit. f_A describes the axion events as shown in Fig. 1 and Fig. 2. The background f_b consists of K-shell X-ray peaks from the cosmogenic nuclides and their corresponding L-shell X-rays and a continuous component with a smooth, slightly increasing profile as the energy decreases. The surface event f_s is derived from fitting the surface spectrum with a smooth curve. The systematic uncertainties of the PDF selection of f_s is negligible by comparing bin by bin PDFs from the f_s spectrum. The number of surface events derived from the Ratio Method is used as ν_s and fixed in the likelihood fit. The results are consistent with the situation in which ν_s is free, but more conservative below 400 eV in the bosonic DM fit. While ν_b and ν_A fitted as free parameters are the numbers of background events and axion events, respectively.

2. Constraints and Systematic uncertainties

\mathcal{L}_2 is a constraint term which encodes prior constraints on the combined efficiencies ε_{eff} ,

$$\mathcal{L}_2 = \exp\left[-\frac{1}{2} \sum_{i,j=1}^2 (e_i - \mu_{ei}) \mathbf{V}_{ij}^{-1} (e_j - \mu_{ej})\right] \times \exp\left[-\frac{1}{2} \sum_{i,j=3}^5 (e_i - \mu_{ei}) \mathbf{V}_{ij}^{-1} (e_j - \mu_{ej})\right]. \quad (18)$$

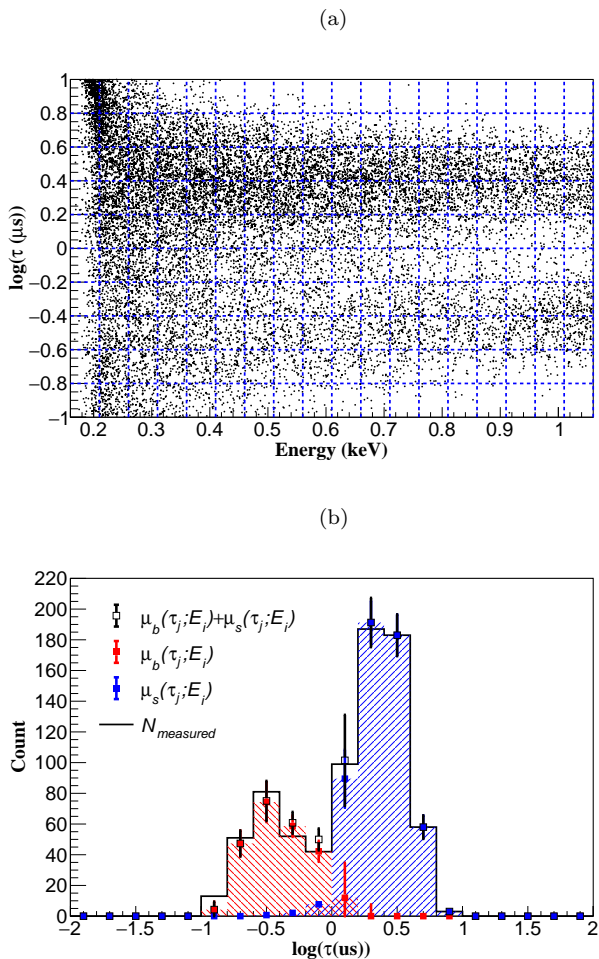


FIG. 5. (a) The event distribution in the rise time vs energy and the blue dashed grid displayed here shows the method of binning. (b) The distribution of rise time in energy bin 0.66 to 0.71 keV. The μ_b and μ_s are the normalized PDFs of bulk and surface events in this energy bin derived from the output of Ratio Method and properly scaled to be compared with the measured numbers.

The five parameters \vec{e} used in two error functions to describe the trigger efficiency and selection efficiency included in ε_{eff} are constrained by \mathcal{L}_2 , with 2D and 3D Gaussians respectively. Both centers of the Gaussians are derived by the best-fit values of parameters denoted $\vec{\mu}_e$ depicted in Fig. 3, and their shapes are determined by the covariance matrix \mathbf{V} between the best-fit values.

According to the evaluation in the previous work [34], one of the dominated uncertainties at the energy range below 1 keV, including statistical and systematic errors, originate from the bulk surface event selection, i.e., the nuisance parameters $g_k(\tau_j; E_i)$, in likelihood function \mathcal{L}_1 . In order to take this uncertainties into consideration, \mathcal{L}_3 term is introduced,

$$\mathcal{L}_3 = e^{-t_b^2/2} \times e^{-t_s^2/2}, \quad (19)$$

which has been parametrized with two parameters t_b, t_s . The likelihood function is defined to be a product of two normally Gaussian distributions, corresponding to where $t = \pm 1$ corresponds to a $\pm 1\sigma$ deviation in $g_k(\tau_j; E_i)$.

The uncertainties of the background assumption are evaluated by using different continuous component in the background assumption between different combinations of exponential, polynomial and flat functions for the fit below 12 keV. For the energy range around 14.4 keV, background assumptions are varied between polynomial, flat and exponential function. The variation of background models causes the change of constraints less than 8% for CBRD axion, less than 16% for bosonic DM, and less than 8% for ^{57}Fe solar axion. As for the uncertainties of resolution, varying the energy resolution by $\pm 10\%$, the changes of results are less than 17% for ^{57}Fe solar axion, less than 13% for bosonic DM and negligible for CBRD axion.

IV. AXION SENSITIVITY ANALYSIS AND RESULTS

A. 14.4 keV Solar Axion

The signal of solar axions produced in the ^{57}Fe magnetic transition on the spectrum is a monochromatic Gaussian peak around 14.4 keV with width determined by resolution, which is about 84 eV (σ) under this situation. The fitting range is limited to 14.06 keV to 14.76 keV, about $\pm 4\sigma$, and a polynomial function is used to describe the background in this range. The 90% C.L. result is shown in Fig. 6 and the rate of this kind of axion is found to be less than $0.029 \text{ counts}\cdot\text{kg}^{-1}\cdot\text{day}^{-1}$. For a low-mass axion at 0 keV, this result translates to a 90% C.L. constraint on the coupling:

$$g_{AN}^{\text{eff}} \times g_{Ae} < 4.14 \times 10^{-17}. \quad (20)$$

Scanning the axion mass from 0 keV to 14.4 keV, we obtained the model-independent limit of $g_{AN}^{\text{eff}} \times g_{Ae}$ shown in Fig. 7.

Within the framework of a specific axion model, KSVZ or DFSZ, the limits on the couplings g_{Ae} can constrain axion mass m_A directly. Using the assumption of parameters mentioned in section II (B), CDEX-1B excludes the mass range $7.3 \text{ eV}/c^2 < m_A < 14.4 \text{ keV}/c^2$ for DFSZ axions, and $141.2 \text{ eV}/c^2 < m_A < 14.4 \text{ keV}/c^2$ for KSVZ axions.

B. CBRD

For CBRD solar axions, the fitting range is from 0.8 keV to 2.0 keV, and there is a saw-tooth-like profile arising in this energy range which is different from the continuous background. Using the analysis procedure mentioned above, we get the constraints on g_{Ae} :

$$g_{Ae} < 2.48 \times 10^{-11}. \quad (21)$$

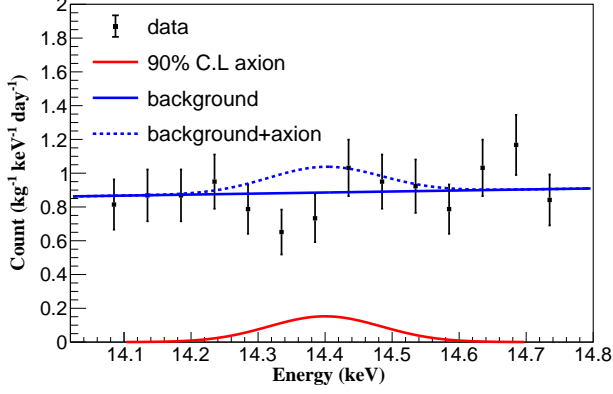


FIG. 6. The bulk data (black data points) and the background assumption (solid blue line), as well as the 90% C.L. ^{57}Fe result (solid red line). The dashed blue line represents the background + 90% C.L. signal.

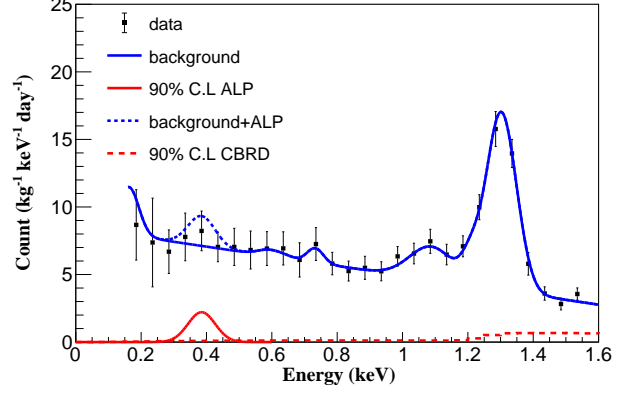


FIG. 8. The bulk data (black data points) and the background assumption (solid blue line) below 1.6 keV, as well as the 90% C.L. ALPs result (solid red line) at mass of 385 eV and the 90% C.L. CBRD result (dashed red line). The dashed blue line is the background + 90% C.L. ALP signal.

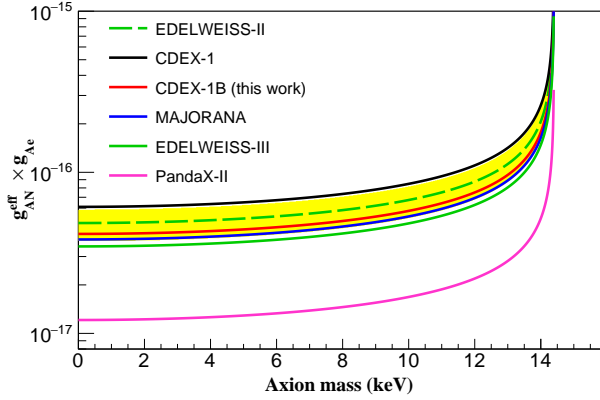


FIG. 7. 90% C.L. upper limit for the model independent coupling of $g_{AN}^{\text{eff}} \times g_{Ae}$ of ^{57}Fe 14.4 keV solar axion (solid red line), compared with CDEX-1A [18], EDELWEISS-II [12], EDELWEISS-III [20], Majorana Demonstrator [14] and PandaX-II [16]. The yellow band represents the 1σ expected sensitivity.

Fig. 8 depicts the fitting results of 90% C.L. This result, together with other experimental bounds, is displayed in Fig. 9. This result excludes the axion masses $m_A > 0.9$ eV/ c^2 in the DFSZ model or $m_A > 257.3$ eV/ c^2 in the KFSZ model, which is better than the result of CDEX-1A.

C. Bosonic Dark Matter

For bosonic dark matter, the fitting range is from 0.16 keV to 11.66 keV and Fig. 8 displays the fitting results at the mass of 385 eV as well as the background model below 1.6 keV. Because of the monochromatic signal, better energy resolution and larger exposure, the CDEX-1B gives us much better results of bosonic DM comparing

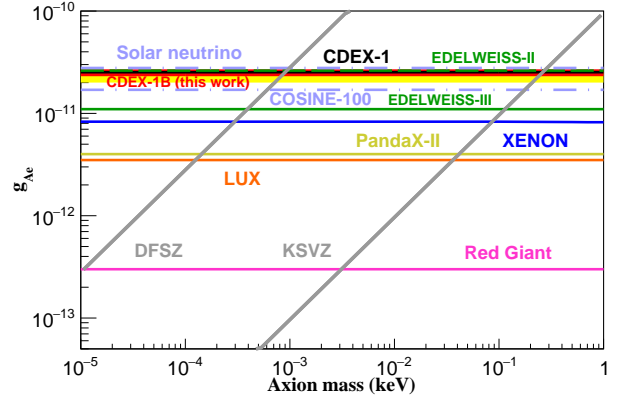


FIG. 9. The CDEX-1B 90% C.L. on CBRD solar axions (solid red line), together with astrophysical bounds [8, 11] and other direct search experiments [12, 15–17, 20, 23]. The yellow band represent the 1σ expected sensitivity.

with CDEX-1A. The 90% C.L. limits on g_{Ae} of ALPs and α'/α of vector bosonic DM are displayed in Fig. 10 and Fig. 11 respectively. Due to the lower energy threshold, we can extend the first point of exclusion line down to the 185 eV.

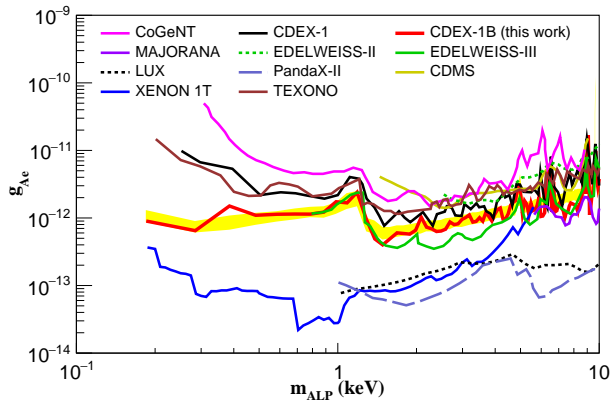


FIG. 10. The CDEX-1B 90% C.L. upper limit on coupling of ALPs as a function of m_{ALP} , together with the constraints set by CDEX-1A [18] and other experiments [9, 10, 12, 14–16, 20–22]. The yellow band represents the 1σ expected sensitivity.

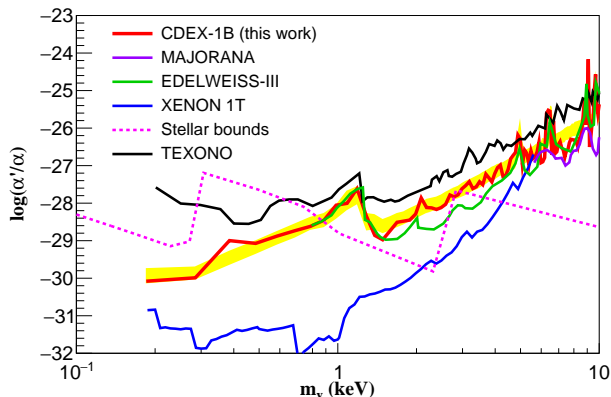


FIG. 11. The 90% C.L. upper limit on the coupling of vector bosonic DM from CDEX-1B together with the result of EDELWEISS-III [20], Majorana Demonstrator [14], XENON 1T [22], TEXONO [21] and astrophysical bounds from [13]. The yellow band represents the 1σ expected sensitivity.

V. SUMMARY

Tighter constraints on the couplings of solar axions and bosonic DM are obtained from CDEX-1B data with an exposure of 737.1 kg-days. Competitive results at the mass of sub-keV of ALPs and vector bosonic DM have been achieved by the help of lower energy threshold and excellent energy resolution measured by the germanium detectors.

These results demonstrate that the profile likelihood ratio method successfully derived the upper limits for our CDEX-1B data in the presence of backgrounds based on the bulk/surface rise-time distribution PDFs. This statistical model takes the main systematic uncertainties, including bulk/surface selection and combined efficiencies, into account through the construction of the likelihood function. The aim of the analysis developed is to provide a reliable statistical forecast of positive signals.

The CDEX-10 detector array with a target mass of the range 10 kg has provided results on low-mass WIMP searches [27] and will be installed in a new 1700 m³ large LN₂ at CJPL-II [25]. In the meantime, the home-made germanium detectors with ultra-low-background electronics are being pursued, which establishes a platform to study the crucial technologies and foresees to suppress the background.

ACKNOWLEDGMENTS

This work is supported by the National Key Research and Development Program of China (No. 2017YFA0402200), the National Natural Science Foundation of China (No. 11505101, 11725522, 11675088, 11475099 and 11475092), the Fundamental Research Funds for the Central Universities (No. 20822041C4030) and Tsinghua University Initiative Scientific Research Program (Grant No. 20197050007).

The authors of affiliations 5 and 11 participated as members of TEXONO Collaboration.

-
- [1] R. D. Peccei and H. R. Quinn, *Phys. Rev. D* **16**, 1791 (1977).
 - [2] S. Weinberg, *Phys. Rev. Lett.* **40**, 223 (1978).
 - [3] F. Wilczek, *Phys. Rev. Lett.* **40**, 279 (1978).
 - [4] J. E. Kim, *Phys. Rev. Lett.* **43**, 103 (1979).
 - [5] M. Shifman, A. Vainshtein, and V. Zakharov, *Nucl. Phys. B* **166**, 493 (1980).
 - [6] M. Dine, W. Fischler, and M. Srednicki, *Phys. Lett. B* **104**, 199 (1981).
 - [7] A. R. Zhitnitskiy, *Yad. Fiz.* **31**, 497 (1980).
 - [8] P. Gondolo and G. G. Raffelt, *Phys. Rev. D* **79**, 107301 (2009).
 - [9] Z. Ahmed *et al.* (CDMS Collaboration), *Phys. Rev. Lett.* **103**, 141802 (2009).
 - [10] C. E. Aalseth *et al.* (CoGeNT Collaboration), *Phys. Rev. Lett.* **106**, 131301 (2011).
 - [11] N. Viaux *et al.*, *Phys. Rev. Lett.* **111**, 231301 (2013).
 - [12] E. Armengaud *et al.* (EDELWEISS Collaboration), *J. Cosmol. Astropart. Phys.* **2013**, 067 (2013).
 - [13] H. An *et al.*, *Phys. Lett. B* **747**, 331 (2015).
 - [14] N. Abgrall *et al.* (Majorana Collaboration), *Phys. Rev. Lett.* **118**, 161801 (2017).
 - [15] D. S. Akerib *et al.* (LUX Collaboration), *Phys. Rev. Lett.* **118**, 261301 (2017).
 - [16] C. Fu *et al.* (PandaX-II Collaboration), *Phys. Rev. Lett.* **119**, 181806 (2017).
 - [17] E. Aprile *et al.* (XENON Collaboration), *Phys. Rev. D* **95**, 029904 (2017).

- [18] S. K. Liu *et al.* (CDEX Collaboration), Phys. Rev. D **95**, 052006 (2017).
- [19] E. Aprile *et al.* (XENON Collaboration), Phys. Rev. D **96**, 122002 (2017).
- [20] E. Armengaud *et al.* (EDELWEISS Collaboration), Phys. Rev. D **98**, 082004 (2018).
- [21] M. K. Singh *et al.*, Chin. J. Phys **58**, 63 (2019).
- [22] E. Aprile *et al.* (XENON Collaboration), Phys. Rev. Lett. **123**, 251801 (2019).
- [23] P. Adhikari *et al.*, Astropart. Phys. **114**, 101 (2020).
- [24] K. J. Kang *et al.*, Front. Phys. **8**, 412 (2013).
- [25] J. P. Cheng *et al.*, Annu. Rev. Nucl. Part. Sci. **67**, 231 (2017).
- [26] Q. Yue *et al.* (CDEX Collaboration), Phys. Rev. D **90**, 091701 (2014).
- [27] H. Jiang *et al.* (CDEX Collaboration), Phys. Rev. Lett. **120**, 241301 (2018).
- [28] L. Wang *et al.* (CDEX Collaboration), Sci. China-Phys. Mech. Astron **60**, 071011 (2017).
- [29] Z. Z. Liu *et al.* (CDEX Collaboration), Phys. Rev. Lett. **123**, 161301 (2019).
- [30] L. T. Yang *et al.* (CDEX Collaboration), Phys. Rev. Lett. **123**, 221301 (2019).
- [31] Y. Wu *et al.*, Chin. Phys. C **37**, 086001 (2013).
- [32] W. Zhao *et al.* (CDEX Collaboration), Phys. Rev. D **88**, 052004 (2013).
- [33] W. Zhao *et al.* (CDEX Collaboration), Phys. Rev. D **93**, 092003 (2016).
- [34] L. T. Yang *et al.* (CDEX Collaboration), Chin. Phys. C **42**, 023002 (2018).
- [35] J. L. Ma *et al.*, Appl. Radiat. Isot. **127**, 130 (2017).
- [36] D. B. Kaplan, Nucl. Phys. B **260**, 215 (1985).
- [37] M. Srednicki, Nucl. Phys. B **260**, 689 (1985).
- [38] S. Andriamonje *et al.*, J. Cosmol. Astropart. Phys. **2009**, 002 (2009).
- [39] J. Redondo, J. Cosmol. Astropart. Phys. **2013**, 008 (2013).
- [40] A. M. Green, Mod. Phys. Lett. A **27**, 1230004 (2012).
- [41] F. Alessandria *et al.*, J. Cosmol. Astropart. Phys. **2013**, 007 (2013).
- [42] A. Derevianko *et al.*, Phys. Rev. D **82**, 065006 (2010).
- [43] M. Pospelov *et al.*, Phys. Rev. D **78**, 115012 (2008).
- [44] L. T. Yang *et al.*, Nucl. Instr. Meth. Phys. Res. A **886**, 13 (2018).
- [45] J. N. Bahcall, Phys. Rev. **132**, 362 (1963).
- [46] W. Bambynek *et al.*, *Orbital electron capture by the nucleus*, Tech. Rep. (1976).
- [47] G. Cowan *et al.*, Europ. Phys. J. C **71**, 1554 (2011).
- [48] A. L. Read, J. Phys. G: Nucl. Part. Phys. **28**, 2693 (2002).